

Low-loss, high-coherence airbridge interconnects fabricated by single-step lithography

Ji-Bang Fu(付济邦), Bo Ren(任波), Jian-Dong Ouyang(欧阳剑东), Cong Li(李璁), Ke-Cheng-Qi Zhu(朱可承琪), Yong-Gang Che(车永刚), Xiang Fu(付祥), Shi-Chuan Xue(薛诗川), Zhao-Hua Yang(杨钊华)†, Ming-Tang Deng(邓明堂)‡, and Jun-Jie Wu(吴俊杰)

Citation: Chin. Phys. B, 2026, 35 (**4**): 040312. DOI: 10.1088/1674-1056/ae50e2
http://cpb.iphy.ac.cn; http://iopscience.iop.org/cpb

What follows is a list of articles you may be interested in

Efficient characterization of the coupler spectrum via sideband driving in superconducting qubits

Jianwen Xu(徐建文), Ruonan Guo(郭若男), Wen Zheng(郑文), Yu Zhang(张钰), Jie Zhao(赵杰), Zhiguo Huang(黄智国), Jingwei Wen(闻经纬), Runqing Zhang(张润清), Shaoxiong Li(李邵雄), Xinsheng Tan(谭新生), and Yang Yu(于扬)

Chin. Phys. B, 2025, 34 (**11**): 110302. DOI: 10.1088/1674-1056/ae00b0

All-microwave CZ gate based on fixed-frequency driven coupler

Wanpeng Gao(高万鹏), Xiaoliang He(何潇梁), Zhengqi Niu(牛铮琦), Daqiang Bao(包大强), Kuang Liu(刘匡), Junfeng Chen(陈俊锋), Zhen Wang(王镇), and Z. R. Lin(林志荣)

Chin. Phys. B, 2025, 34 (**4**): 040304. DOI: 10.1088/1674-1056/adb68a

In situ non-destructive measurement of Josephson junction resistance using fritting contact technique

Lei Du(杜磊), Hao-Ran Tao(陶浩然), Liang-Liang Guo(郭亮亮), Hai-Feng Zhang(张海峰), Yong Chen(陈勇), Xin Tian(田昕), Chi Zhang(张驰), Zhi-Long Jia(贾志龙), Peng Duan(段鹏), and Guo-Ping Guo(郭国平)

Chin. Phys. B, 2024, 33 (**11**): 110309. DOI: 10.1088/1674-1056/ad73b6

Diagnosing quantum crosstalk in superconducting quantum chips by using out-of-time-order correlators

Yujia Zhang(张宇佳), Yu Zhang(张钰), Shaoxiong Li(李邵雄), Wen Zheng(郑文), and Yang Yu(于扬)

Chin. Phys. B, 2024, 33 (**11**): 110306. DOI: 10.1088/1674-1056/ad73b3

Remote entangling gate between a quantum dot spin and a transmon qubit mediated by microwave photons

Xing-Yu Zhu(朱行宇), Le-Tian Zhu(朱乐天), Tao Tu(涂涛), and Chuan-Feng Li(李传锋)

Chin. Phys. B, 2024, 33 (**2**): 020315. DOI: 10.1088/1674-1056/ad1747

Low-loss, high-coherence airbridge interconnects fabricated by single-step lithography

Ji-Bang Fu(付济邦), Bo Ren(任波), Jian-Dong Ouyang(欧阳剑东), Cong Li(李璁), Ke-Cheng-Qi Zhu(朱可承琪), Yong-Gang Che(车永刚), Xiang Fu(付祥), Shi-Chuan Xue(薛诗川), Zhao-Hua Yang(杨钊华)[†], Ming-Tang Deng(邓明堂)[‡], and Jun-Jie Wu(吴俊杰)

College of Computer Science and Technology, National University of Defense Technology, Changsha 410073, *China*

(Received 29 January 2026; revised manuscript received 5 March 2026; accepted manuscript online 12 March 2026)

Airbridges are essential for creating high-performance, low-parasitic interconnects in integrated circuits and quantum devices. Conventional multi-step fabrication methods hinder miniaturization and introduce process-related defects. We report a simplified process that enables the fabrication of nanoscale airbridges with just one step of electron-beam lithography. By optimizing a multilayer resist stack with a triple-exposure-dose scheme and a thermal reflow step, we achieve burr-free, suspended metallic bridges with sub-micron features that exhibit robust mechanical stability. Fabricated within a gradiometric SQUID design for superconducting transmon qubits, these airbridges introduce no measurable additional loss in the relaxation time T_1, while enabling a 2.5-fold enhancement of the dephasing time T_2^*. This efficient method offers a practical route toward integrating high-performance three-dimensional interconnects in advanced quantum and nano-electronic devices.

Keywords: superconducting qubit, airbridge fabrication, superconducting device

PACS: 03.67.Lx, 81.07.–b, 85.25.–j, 85.25.Am

DOI: 10.1088/1674-1056/ae50e2 **CSTR:** 32038.14.CPB.ae50e2

1. Introduction

The continuous drive for miniaturization, increased functionality, and superior performance in modern integrated circuits, photonic integrated circuits, and microelectromechanical systems necessitates the development of complex three-dimensional architectures. A critical challenge is creating high-performance, low-parasitic interconnections that can span over underlying components or other interconnect layers without introducing detrimental electrical, optical, or mechanical interference. Airbridge structures are an indispensable enabling technology for this purpose.[1–4] In quantum information processing, airbridges are particularly important for realizing low-loss microwave resonators, essential coupling elements between qubits, and effective grounding strategies that suppress spurious electromagnetic modes, thereby directly enhancing qubit coherence and gate fidelity.[5–9]

Conventional airbridge fabrication typically relies on multi-layer resist stacks and multiple lithography steps to define suspended metallic structures after selective etching of a sacrificial layer.[10–14] While functional, these methods require complex alignment across exposures and risk introducing organic residues or process-induced defects that can degrade quantum coherence,[15,16] thereby hindering further miniaturization and high-density integration. Alternative single-step methods, such as gradient exposure[17] or two-photon lithography,[8] can form arched bridge profiles but face challenges in scaling to sub-micron dimensions.

Here, we present a method for fabricating airbridges using only a single electron-beam lithography (EBL) step. By optimizing a multilayer resist composition and applying a triple-exposure-dose scheme followed by a thermal reflow, we achieve an undercut profile that yields burr-free, suspended metallic bridges after development and lift-off. These single-lithography airbridges (SL-airbridges) feature sub-micron dimensions, a well-defined arch shape, and strong resilience to low-power ultrasonic treatment. This streamlined process can be directly integrated into quantum circuit fabrication without introducing additional decoherence sources.

2. Experimental setup

The SL-airbridge fabrication sequence is illustrated in Fig. 1. We start by introducing the carefully designed electron-beam resist stack. First, a 300-nm-thick layer of poly(methyl methacrylate) (PMMA, 950k molecular weight) is spin-coated on a substrate and baked at 160 °C for 10 min. This bottom layer defines the electrical contact region between the airbridge and the underlying circuit. Next, a 400-nm-thick layer is spin-coated and baked under the same conditions. Finally, a 400-nm-thick blended resist layer, composed of PMMA and MMA in a 2:3 ratio, is spin-coated and baked. The blended top layer offers higher sensitivity than that of pure PMMA for forming the bridge profile while maintaining pattern stability during the subsequent thermal reflow.

[†]Corresponding author. E-mail: zhaohuayang@quanta.org.cn

[‡]Corresponding author. E-mail: mtdeng@nudt.edu.cn

© 2026 Chinese Physical Society and IOP Publishing Ltd. All rights, including for text and data mining, AI training, and similar technologies, are reserved.

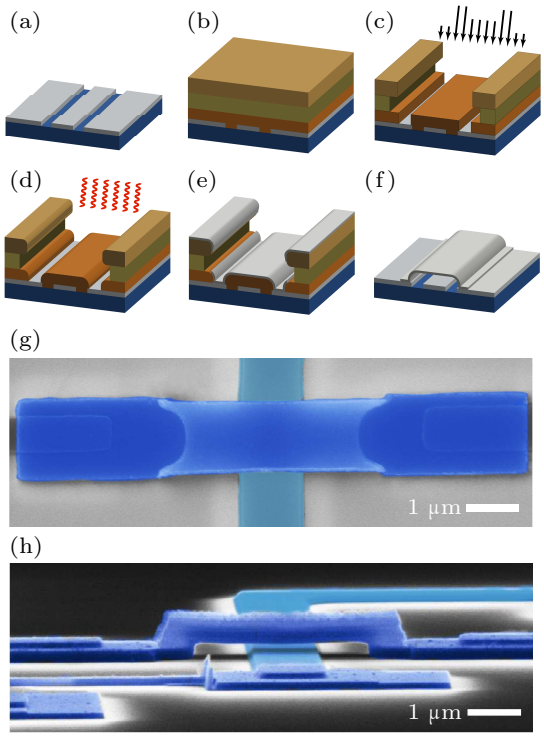


Fig. 1. Schematic of the single-lithography airbridge (SL-airbridge) fabrication process. (a) Deposition, patterning, and etching of a 100-nm-thick Al base wire. (b) Spin-coating of a multilayer electron-beam resist stack. (c) Patterning via EBL using three distinct exposure doses. (d) Thermal reflow of the developed resist stack on a hotplate. (e) Ion milling of the base metal contact areas followed by electron-beam evaporation of the bridge metal (150 nm Al). (f) Lift-off and ultrasonic cleaning. (g) Top-view scanning electron microscopy (SEM) image of a fabricated nanoscale airbridge. (h) Side-view SEM image of an airbridge taken at an 85° stage tilt.

Patterning is performed using standard EBL. A critical aspect is the application of three calibrated exposure doses. The highest dose (exceeding 1000 μC/cm^2) fully exposes the entire resist stack to define the airbridge pedestal. An intermediate dose (300–500 μC/cm^2) exposes the MMA and PMMA/MMA blend layers to pattern the suspended bridge profile. The lowest dose (below 150 μC/cm^2) is designed to create a controlled undercut within the middle MMA layer, which is crucial for successful lift-off after reflow.

After exposure, the sample is developed in a 1:3 mixture of methyl isobutyl ketone and isopropyl alcohol (MIBK:IPA) for 45 s. A thermal reflow step is then performed at 125 °C, the glass transition temperature of PMMA, for a precisely controlled duration of 45 s. This step transforms the developed profile into a smooth, arched shape essential for continuous metal deposition.

Metallization begins with standard argon ion milling to clean the contact areas and ensure low-resistance interfaces, followed by electron-beam evaporation of a 150-nm-thick aluminum film at normal incidence. Lift-off is carried out in an 80 °C N-methyl-2-pyrrolidone (NMP) bath. Low-power ultrasonic agitation is applied to remove edge residues and improve the smoothness of the bridge.

Figures 1(g) and 1(h) show representative SEM images of a completed SL-airbridge, which is 2 μm wide and approximately 200 nm high. The burr-free edges indicate a high-quality lift-off process.

A previously reported single-step lithography method using a triple-layer PMMA/MMA stack employed only two exposure doses and omitted thermal reflow.[18] The resulting airbridges exhibited rough edges, which could increase surface loss and electromagnetic radiation, thereby degrading quantum coherence. Furthermore, such structures could not tolerate ultrasonic cleaning, limiting their use in complex fabrication sequences.

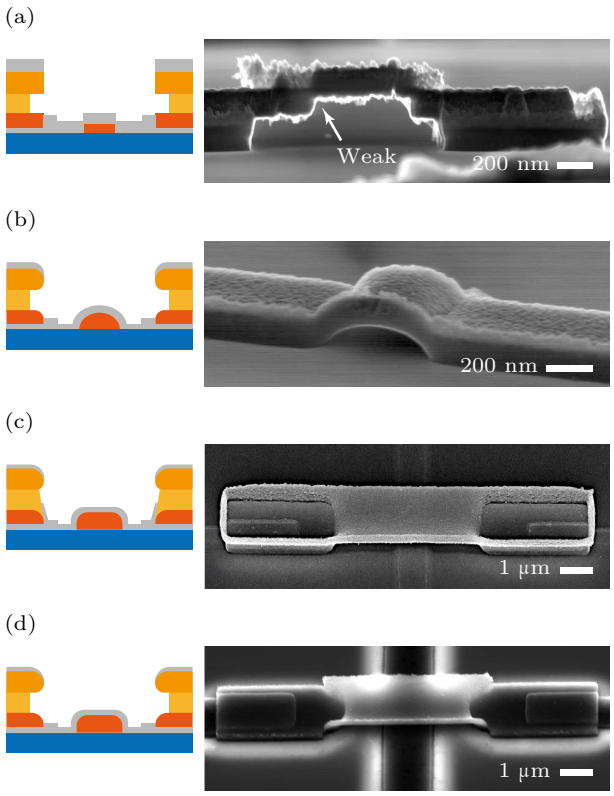


Fig. 2. Comparison of SL-airbridges (400 nm width) fabricated (a) without and (b) with the thermal reflow step and comparison of SL-airbridges (2 μm width) fabricated (c) with a double-dose exposure scheme and (d) with the optimized triple-dose exposure scheme.

To highlight the importance of thermal reflow and the triple-dose strategy, we performed control experiments, shown in Fig. 2. Without reflow, the deposited metal layers show rough edges and discontinuous connections [Fig. 2(a)]. With reflow, the SL-airbridge maintains a burr-free profile even at sub-micron scales [Fig. 2(b)]. However, reflow alone tends to reduce the undercut, complicating lift-off and leading to raised metal walls, as seen in Fig. 2(c). The triple-dose exposure scheme resolves this conflict by using a low dose to preserve a controlled undercut in the MMA layer after reflow. Airbridges fabricated with a double-dose scheme exhibit unstable, raised edges due to the resist slope [Fig. 2(c)], whereas the triple-dose scheme yields burr-free, well-defined edges [Fig. 2(d)]. The current smallest SL-airbridge can reach 200 nm width. Further

reducing the width is currently not feasible because the thermal reflow of the photoresist during the processing will cause the patterned features to expand, thus preventing the formation of such a narrow gap.

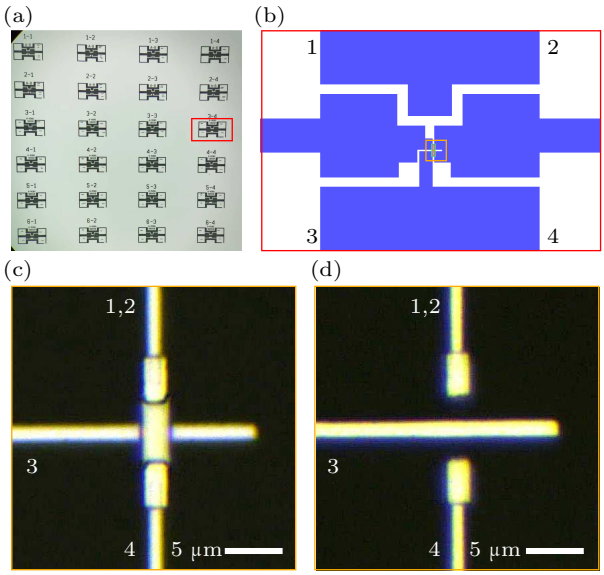


Fig. 3. Ultrasonic treatment tests of SL-airbridges. (a) Optical images of a subset of the 60 test samples. (b) Layout of a single test sample with four contact pads. (c) Intact SL-airbridge after low-power ultrasonic treatment for 20 s. (d) Damaged SL-airbridge after high-power ultrasonic treatment for 20 s.

The robustness of the SL-airbridge against ultrasonic processing, a common step in superconducting device fabrication, was systematically evaluated. We prepared 60 test samples, each containing four electrode pads for electrical characterization [Figs. 3(a) and 3(b)]. Pads 1 and 2 are electrically shorted through the airbridge. Conductivity between pad 1 (or 2) and pad 4 confirms the airbridge's electrical integrity, while resistance between pad 1 (or 2) and pad 3 checks for shorts indicative of collapse or damage. All SL-airbridges on the sample are 5 μm in length and 2 μm in width. Samples were treated in an ultrasonic cleaner (Branson 3800) for 20 s in low-power mode. All 60 samples survived intact [Fig. 3(c)]. When treated for 20 s in high-power mode, approximately 30% of the airbridges were damaged [Fig. 3(d)], demonstrating a practical operating limit. When the length of the SL-airbridge extends beyond 5 μm, the increase in van der Waals forces between the bridge and the substrate may lead to collapse during the ultrasonic cleaning process.

3. Results and discussion

To demonstrate the utility of SL-airbridges in quantum devices, we implemented them in a novel transmon qubit design featuring a doubly connected gradiometric superconducting quantum interference device (SQUID), termed the "8-mon".[19] This design aims to enhance coherence by canceling quasi-static flux noise while preserving frequency tunability. As shown in the false-colored SEM image in Fig. 4(a), an SL-airbridge connects the two loops of the gradiometric SQUID.

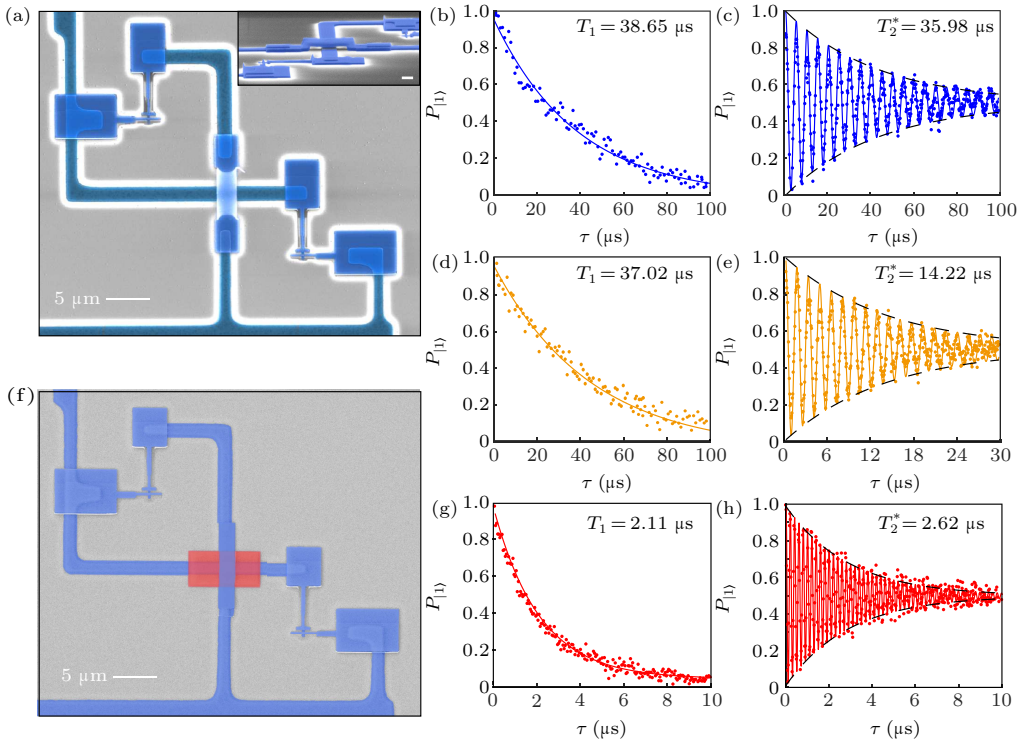


Fig. 4. Enhanced qubit coherence with SL-airbridge interconnects. (a) False-color SEM image of an 8-mon qubit with an SL-airbridge (blue) connecting the two loops of the gradiometric SQUID. Inset shows a side-view SEM image at a 75° tilt. (b) Highest measured T_1 of 8-mon with SL-airbridge (data from Q_1). (c) Highest measured T_2^* of 8-mon with SL-airbridge (data from Q_1). (d) Highest measured T_1 of control group X-mon (data from Q_4). (e) Highest measured T_2^* of control group X-mon (data from Q_4). (f) False-color SEM image of an 8-mon qubit with a dielectric (SiO_2, red) crossover. (g) Highest measured T_1 of 8-mon with dielectric crossover (data from Q_6). (h) Highest measured T_2^* of 8-mon with dielectric crossover (data from Q_6).

Table 1. Summary of single-qubit parameters from coherence measurements. Values are averages over more than 10 measurements. ω^{idle} is the idle frequency, and ω^{R} is the readout resonator frequency.

Qubit	$\omega^{\mathrm{idle}}/2\pi$ (GHz)	$\omega^{\mathrm{R}}/2\pi$ (GHz)	$\bar{T}_1$ (μs)	$\bar{T}_2^*$ (μs)
Q_1 [a]	5.028	6.430	33.70	32.40
Q_2 [a]	4.473	6.286	33.57	27.73
Q_3 [a]	4.426	6.384	26.57	26.51
Q_4 [b]	5.397	6.615	27.91	13.05
Q_5 [b]	4.954	6.572	22.82	11.48
Q_6 [c]	4.448	6.271	1.96	2.34
Q_7 [c]	4.911	6.222	1.88	1.30
Q_8 [c]	4.993	6.415	1.53	1.63

[a] 8-mon qubit with an SL-airbridge crossover. [b] X-mon qubit.
[c] 8-mon qubit with a dielectric (SiO_2) crossover.

We co-fabricated 8-mon qubits and conventional X-mon qubits on the same chip and measured their coherence properties under identical conditions. Results for selected qubits are summarized in Table 1, with all data averaged over more than 10 measurement repetitions. The T_1 times of the 8-mons are comparable to those of the X-mons. Qubit Q_1 (8-mon) achieved a maximum T_1 of 38.65 μs [Fig. 4(b)], indicating that the SL-airbridge introduces no measurable additional relaxation loss. The same qubit reached a maximum T_2^* of 35.98 μs [Fig. 4(c)], approximately 2.5 times that of the X-mon (Q_4, $T_2^* = 14.22$ μs) [Fig. 4(e)]. This confirms the efficacy of the gradiometric design in mitigating dephasing noise. The coherence times of our X-mons are consistent with recent reports.[20–23]

To underscore the low-loss nature of the airbridge interconnect, we fabricated a control sample where the crossover in the 8-mon was formed using a dielectric insulating layer (SiO_2) deposited via electron-beam evaporation at 95 °C [Fig. 4(f)]. The introduction of this amorphous dielectric material severely degraded coherence, reducing both T_1 and T_2^* to approximately 2 μs [Figs. 4(g), 4(h) and Table 1], highlighting the superior performance of the airbridge-based approach.

4. Conclusion

In summary, we have developed a streamlined process for fabricating airbridge interconnects requiring only single-step lithography. The method combines an optimized multilayer resist stack, a triple-exposure-dose scheme, and a thermal reflow step to reliably produce burr-free, suspended metallic bridges with sub-micron features and lengths exceeding 5 μm. Validated in superconducting quantum devices, the SL-airbridge exhibits low loss, high mechanical stability, and full compatibility with standard fabrication workflows. It enables greater design freedom for complex quantum circuit geometries. This approach offers a practical and accessible route to integrate high-performance three-dimensional interconnects in next-generation quantum circuits, photonic devices, and nano-electronics, where minimizing parasitic interactions is paramount to advancing performance and integration density.

Acknowledgements

We thank Yang Yang, Xiao-Feng Yi, Ding-Dong Liu, Peng Luo, and Kang-Ding Zhao for technical support in device fabrication and measurements. Project supported by the National Key R&D Program of China (Grant No. 2024YFB4504000) and the Aid Program for Science and Technology Innovative Research Team in Higher Educational Institutions of Hunan Province. Device fabrication was partially performed at the Synergetic Extreme Condition User Facility (SECUF).

References

[1] Sherwin M E, Simmons J A, Eiles T E, Harff N E and Klem J F 1994 *Appl. Phys. Lett.* **65** 2326
[2] Villeneuve P R, Fan S, Joannopoulos J D, Lim K, Petrich G S, Kolodziejski L A and Reif R 1995 *Appl. Phys. Lett.* **67** 167
[3] Borzenko T, Gould C, Schmidt G and Molenkamp L 2004 *Microelectron. Eng.* **75** 210
[4] Girgis E, Liu J and Benkhedar M L 2006 *Appl. Phys. Lett.* **88** 202103
[5] Chen Z, Megrant A, Kelly J, Barends R, Bochmann J, Chen Y, Chiaro B, Dunsworth A, Jeffrey E, Mutus J Y, O'Malley P J J, Neill C, Roushan P, Sank D, Vainsencher A, Wenner J, White T C, Cleland A N and Martinis J M 2014 *Appl. Phys. Lett.* **104** 052602
[6] Sun Y, Ding J, Xia X, Wang X, Xu J, Song S, Lan D, Zhao J and Yu Y 2022 *Appl. Phys. Lett.* **121** 074001
[7] Stavenga T, Khan S A, Liu Y, Krogstrup P and DiCarlo L 2023 *Appl. Phys. Lett.* **123** 024004
[8] Huang Y H, Wang H, Shen Z, Thomas A, Richardson C J K and Palmer B S 2025 *Appl. Phys. Lett.* **127** 044002
[9] Bolgar A N, Kalacheva D A, Lubsanov V B, Dmitriev A Y, Alekseeva E S, Korostylev E V and Astafiev O V 2025 *J. Appl. Phys.* **137** 154401
[10] Zhang Y, Liu J, Li Y and Yang F 2007 *Mater. Sci. Semicond. Process.* **10** 194
[11] Dunsworth A, Barends R, Chen Y, Chen Z, Chiaro B, Fowler A, Foxen B, Jeffrey E, Kelly J, Klimov P V, Lucero E, Mutus J Y, Neeley M, Neill C, Quintana C, Roushan P, Sank D, Vainsencher A, Wenner J, White T C, Neven H, Martinis J M and Megrant A 2018 *Appl. Phys. Lett.* **112** 063502
[12] Tao H R, Zhang C, Du L, Yang X X, Guo L L, Chen Y, Zhang H F, Jia Z L, Kong W C, Duan P and Guo G P 2024 *Appl. Phys. Lett.* **125** 034001
[13] Bu K, Huai S, Zhang Z, Li D, Li Y, Hu J, Yang X, Dai M, Cai T, Zheng Y C, *et al.* 2025 *npj Quantum Inf.* **11** 17
[14] Bruckmoser N, Koch L, Tsitsilin I, Grammer M, Bunch D, Richard L, Schirk J, Wallner F, Feigl J, Schneider C M F, Geprägs S, Bader V P, Althammer M, Södergren L and Filipp S 2026 *Phys. Rev. Appl.* **25** 024007
[15] Siddiqi I 2021 *Nat. Rev. Mater.* **6** 875
[16] Mahuli N, Minguzzi J, Gao J, Resnick R, Diez S, Cosmic R, Marcaud G, Hunt M, Swenson L, Rose J, Painter O and Jarrige I 2025 *ACS Nano* **19** 41136
[17] Janzen N, Kononenko M, Ren S and Lupascu A 2022 *Appl. Phys. Lett.* **121** 094001
[18] Jin Y, Moreno M, T Vianez P M, Tan W K, Griffiths J P, Farrer I, Ritchie D A and Ford C J B 2021 *Appl. Phys. Lett.* **118** 162108
[19] Fu J B, Wang D W, Ren B, Yang Z H, Hu S, Huang G Y, Cao S H, Liu D D, Zhang X F, Fu X, Xue S C, Che Y G, Liu Y, Deng M T and Wu J J 2026 arXiv:2601.02137 [quant-ph]
[20] Wu Y, Bao W S, Cao S, Chen F, Chen M C, Chen X, Chung T H, Deng H, Du Y, Fan D, Gong M, *et al.* 2021 *Phys. Rev. Lett.* **127** 180501
[21] Shi Y H, Liu Y, Zhang Y R, Xiang Z, Huang K, Liu T, Wang Y Y, Zhang J C, Deng C L, Liang G H, Mei Z Y, Li H, Li T M, Ma W G, Liu H T, Chen C T, Liu T, Tian Y, Song X, Zhao S P, Xu K, Zheng D, Nori F and Fan H 2023 *Phys. Rev. Lett.* **131** 080401
[22] Xiang Z C, Huang K, Zhang Y R, Liu T, Shi Y H, Deng C L, Liu T, Li H, Liang G H, Mei Z Y, *et al.* 2023 *Nat. Commun.* **14** 5433
[23] Wu Z H, Lei L X, Zhang X F, Xue S C, Hu S, Li C, Fu X, Chen P X, Lu K, Deng M T and Wu J J 2025 *Chin. Phys. Lett.* **42** 040501